

Large-Gap Quantum Anomalous Hall Insulators in ATiX Class

Yadong Jiang,¹ Huan Wang,¹ and Jing Wang^{1,2,3,*}

¹State Key Laboratory of Surface Physics and Department of Physics, Fudan University, Shanghai 200433, China

²Institute for Nanoelectronic Devices and Quantum Computing, Fudan University, Shanghai 200433, China

³Zhangjiang Fudan International Innovation Center, Fudan University, Shanghai 201210, China

(Dated: November 18, 2022)

We theoretically propose that the monolayer ATiX family (KTiSb, KTiBi, RbTiSb, SrTiSn) are potential candidates for large-gap quantum anomalous Hall insulators with high Chern number $\mathcal{C} = 2$. Both of the topology and magnetism in these materials are from $3d$ -orbitals of Ti. We construct the tight-binding model with symmetry analysis to reveal the origin of topology. Remarkably, quite different from the conventional s - d band inversion, here the topological band inversion within $3d$ orbitals is due to the crystal field and electron hopping, while spin-orbit coupling only trivially gaps out the Dirac cone at Fermi level. The general physics from the $3d$ orbitals here applies to a large class of transition metal compounds with the space group $P4/nmm$ or $P-42m$ and their subgroups.

Introduction. The precise theoretical prediction and experimental realization of the quantum anomalous Hall (QAH) effect set a remarkable example for understanding and engineering topological states of quantum matter in complex materials [1–6]. The QAH insulator has a topologically nontrivial electronic structure with a finite Chern number [7] characterized by a bulk energy gap but gapless chiral edge states, leading to the quantized Hall effect without an external magnetic field [8]. The QAH effect has been realized in magnetically doped topological insulators (TI) [9–13], in the intrinsic magnetic TI MnBi_2Te_4 [14], in the twisted bilayer graphene [15] and transition metal dichalcogenide heterobilayers [16], with comparable onset temperature of about a few Kelvin. The QAH states have been proposed for low energy cost electronic devices and topological computation [17–19], however, such low critical temperature is a major obstacle for practical applications. Seeking high-temperature QAH insulators [20–25] has become an important goal in condensed matter physics and material sciences.

The general mechanism for QAH insulator is the spin polarized band inversion [26], where both the ferromagnetic (FM) ordering and spin-orbit coupling (SOC) are sufficiently strong. Physically, the ferromagnetism favors transition metal elements with $3d$ electron, while strong SOC prefers heavy elements. These considerations constitute the essential ingredients for QAH effect in magnetic TI by introducing magnetic dopants or intercalating magnetic layer [27–31]. However, the inhomogeneities from magnetic dopants [32] and defects [33] dramatically suppress the exchange gap by several order of magnitude, which fundamentally limits the fully quantized anomalous Hall effect to very low temperatures. The challenge in searching for high-temperature QAH insulators is to synergize the seemingly conflicting requirements of ferromagnetism and SOC.

Here we propose the monolayer ATiX class (KTiSb, KTiBi, RbTiSb, SrTiSn) are potential candidates for large-gap QAH insulators with high-temperature. Their stability, magnetic, electronic, and topological properties

are comprehensively investigated by first principles calculations. Remarkably, these materials have Chern number $\mathcal{C} = 2$ in the FM ground state, where topology and magnetism are purely from d -orbitals of Ti. We further construct the tight-binding model from orbital projected band structure and symmetry analysis to reveal the origin of topology. Remarkably, the band inversion is due to tetrahedral crystal field and hopping, while SOC only trivially gap out the Dirac cone at Fermi level. The general physics from the $3d$ orbitals here applies to material class of transition metal compounds with the space group $P4/nmm$ or $P-42m$ and their subgroups.

Structure and magnetic properties. The monolayer ATiX class has a tetragonal lattice with the space group $P4/nmm$ (No. 129), similar to LiFeSe [22]. As shown in Fig. 1(a), each primitive cell includes five atomic layers, where each Ti atom is surrounded by four X atoms form-

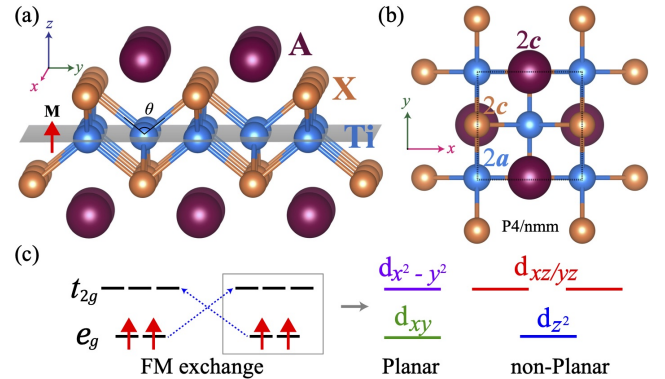


FIG. 1. (a) and (b) Side and top views of ATiX monolayer. The 2D material class has a FM ground state along z axis with spin magnetic moment $2\mu_B$ per Ti atom. θ is bond angle of X -Ti- X . The Wyckoff positions $2a$ and $2c$ are displayed (notation adopted from Bilbao Crystallographic Server [34–36]). The key symmetry operations include C_{4z} rotation, M_x and M_y mirrors, C_{2x} and C_{2y} rotations. (c) Crystal field splitting and schematic diagram of the FM kinetic exchange coupling between Ti atoms.

	a (Å)	θ (°)	MAE (meV)	T_c (K)
KTiSb	4.49	101	2.6	637
KTiBi	4.56	99	9.8	662
RbTiSb	4.53	103	2.0	598
SrTiSn	4.50	98	1.0	436

TABLE I. Lattice constants, bond angle, MAE per unit cell, and Curie temperature T_c from Monte Carlo simulations.

ing a distorted edge-sharing tetrahedron, and the group IA (or IIA) element A with an ultralow electronegativity easily loses valence electrons and becomes A^+ (or A^{2+}). These QAH materials are obtained from high-throughput screening of insulating $ATiX$ with X from group IVA and VA. Their lattice constants are listed in Table I. The absence of imaginary phonon frequency from the phonon spectra calculations suggest the dynamical stability of monolayer $ATiX$ structure (Fig. S1 [37]). We will mainly discuss KTiSb with similar results for this class.

To determine the magnetic ground state of monolayer $ATiX$, we compare five magnetic configurations: (i) FM, (ii) checkboard antiferromagnetic (AFM), (iii) collinear AFM, (iv) zigzag AFM, and (v) big zigzag AFM (see Fig. S2 [37]), and find that FM is the ground state (Table S1 [37]). Take KTiSb for example, the calculated energy of FM state is about 290, 277, 146, and 205 meV/Ti lower than the four AFM states, respectively. The energy difference is found to be similar for other monolayer $ATiX$. The large magnetic energy difference indicates the FM exchange coupling is strong. The magnetocrystalline anisotropy energy (MAE), defined as the total energy difference between in-plane and out-of-plane spin configurations, are listed in Table I, while a positive MAE implies an out-of-plane easy axis.

To elucidate the underlying mechanism of ferromagnetism, we analyze the orbital occupation of Ti atoms. The d orbitals are split by the tetrahedral crystal field into doublet $e_g(d_{xy}, d_{z^2})$ and triplet $t_{2g}(d_{x^2-y^2}, d_{xz}, d_{yz})$ orbitals (Fig. 1(c) with coordinates in Fig. 1(b)). The energy of e_g stays lower with respect to t_{2g} , because the latter point towards the negatively charged ligands. Each Ti atom is in the $e_g^2 t_{2g}^0$ configuration with the magnetic moment of $2\mu_B$ according to the Hund's rule, which is consistent with the density functional theory calculation. The exchange between two neighboring Ti atoms with closed e_g^2 subshell must be AFM, which is associated with the Pauli exclusion principle in the virtually excited $e_g^1 e_g^3$ state. Meanwhile, the superexchange from near 90° Ti-X-Ti bond leads to extremely weak FM only [38]. The key is rooted in the FM e_g - t_{2g} kinetic exchange, the large radius of ligands only cause small crystal field splitting which further make FM e_g - t_{2g} exchange dominates over AFM e_g - e_g exchange. Furthermore, the *ab initio* Heisen-

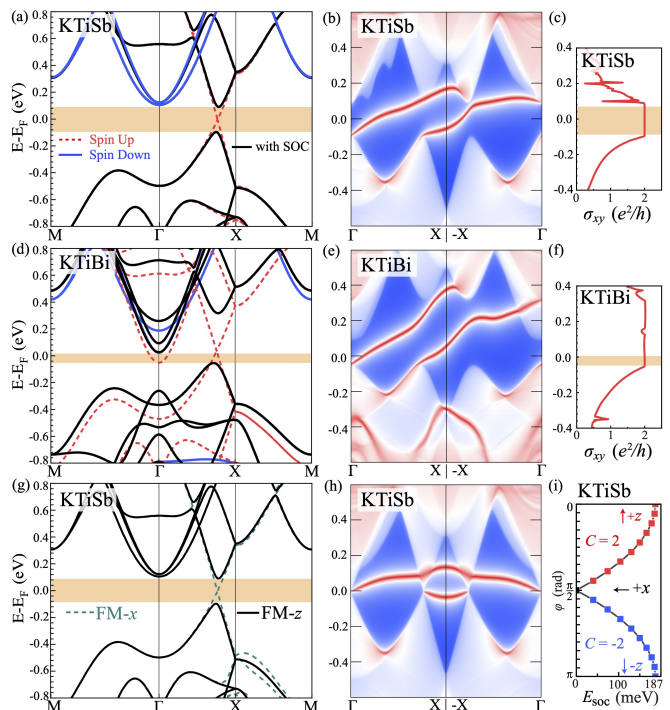


FIG. 2. Electronic structure and topological properties of monolayer KTiSb and KTiBi. (a)-(c) KTiSb, (d)-(f) KTiSb, The band structure with and without SOC; topological edge states calculated along x direction; anomalous Hall conductance σ_{xy} as a function of Fermi energy, respectively. (g) The band structure for FM along z - and x -axis of KTiSb. (h) The edge states along x axis under FM- x state of KTiSb. (i) Dependence of band gap and C on the spin orientation quantified by a polar angle φ , where $\varphi = 0, \pi/2, \pi$ denote the $+z, +x, -z$ directions, respectively.

berg exchange parameters of KTiSb are $J_1 = -72.6$ meV, $J_2 = -33.1$ meV, and $J_3 = 16.4$ meV for nearest-, next-nearest-, and next-nearest-neighbor Ti-Ti pairs, respectively [37]. Negative J_i means the FM exchange coupling. The Curie temperature for monolayer $ATiX$ are listed in Table I (Fig. S3) by Monte Carlo simulations [37].

Electronic structures. Fig. 2(a) displays the electronic structure of monolayer KTiSb with and without SOC. In the absence of SOC, the spin-down bands has an insulating gap, and the spin up bands form a spin polarized Dirac semimetal. Specifically, the two spin-up bands near the Fermi level are mainly contributed by $d_{x^2-y^2}$ and d_{xy} orbitals of Ti (Fig. 3(a)), where the Dirac points along Γ - X (Γ - Y) are protected by M_y (M_x). When including SOC, the out-of-plane ferromagnetism breaks M_x and M_y , and SOC opens a Dirac gap. The anomalous Hall conductance σ_{xy} as a function of Fermi energy is calculated in Fig. 2(c), which displays a quantized value of $2e^2/h$ within the bulk gap of 187 meV. This indicates the topological nontrivial bands with Chern number $C = 2$, which is consistent with two chiral edge states dispersing within the bulk gap as in the edge local density of states

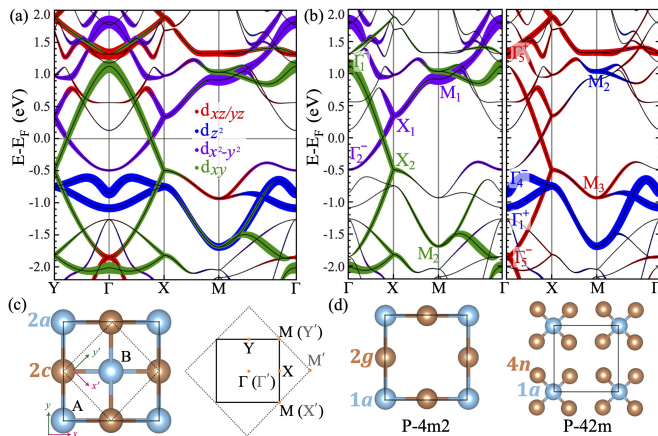


FIG. 3. (a) The d -orbital projected band structures without SOC for spin up of monolayer KTiSb. (b) The IR of high symmetry point at Brillouin zone boundary, where $(d_{xy}, d_{x^2-y^2})$ and $(d_{xz/yz}, d_{z^2})$ are separately displayed. (c) The relation between original (labelled by Γ - X - Y - M) and unfolded Brillouin zone (labelled by Γ' - X' - Y' - M'). Here M' and Γ' are folded into Γ . The coordinates (x, y) and (x', y') are for original and new unit cell, respectively. (d) Lattices of space group $P-4m2$ (No. 115) and $P-42m$ (No. 111).

calculations (Fig. 2(b)). By further varying the spin orientation from $-z$ to $+x$, then to the $+z$ axis, the band gap monotonically decreases to close, and then reopens, which is accompanied by the topological phase transitions from $\mathcal{C} = -2$ to $\mathcal{C} = 2$ in Fig. 2(i). For in-plane ferromagnetism along x axis, the gapless Dirac points along Γ - X (Fig. 2(g)) are protected by C_{2x} , while the Dirac points along Γ - Y are protected by M_x . Electronic structure of monolayer KTiBi with similar topological properties are shown in Fig. 2(d)-2(f), with an indirect band gap of 80 meV. The sizable band gap (Table S2) in this family is attributed to the enhanced effective SOC strength of Ti-3d orbitals by bonding with the ligand heavy elements.

Symmetry and origin of topology. To reveal the origin of $\mathcal{C} = 2$ topology in the electronic structure, we perform a systematic investigation of orbital projected band structure and symmetry analysis of irreducible representations (IR), and further construct a tight-binding model to recover the essential topological physics. Remarkably, different from the conventional s - p or s - d band inversion, where SOC not only induces topological band inversion but also opens the Dirac gap. Here, the band inversion is due to crystal field and hopping, while SOC only trivially gap out the Dirac cone at Fermi level.

The orbital projected (spin up) band structures without SOC is shown in Fig. 3(a). The band inversion between d_{xy} and $d_{x^2-y^2}$ at Fermi level induces four Dirac points, which are gapped by SOC. Naively, these features seem to explain $\mathcal{C} = 2$ phase well with each gapped Dirac point contributing $\mathcal{C} = 1/2$. However, by calcu-

lating IR of the inverted bands at Γ (Fig. 3(b) left), we find that IR of the two bands Γ_1^- and Γ_2^- have the same C_{4z} eigenvalue 1 (see character table in Table S3), which indicate the band inversion between d_{xy} and $d_{x^2-y^2}$ is trivial and does not contribute Chern number. We further write down a tight-binding model from the *planar* orbitals $(d_{xy}, d_{x^2-y^2})$ as $\mathcal{H}_1 = \sum_{\langle ij \rangle} [d_i^\dagger \hat{t}_{ij} d_j + \text{H.c.}] + \sum_{\langle\langle ij \rangle\rangle} [d_i^\dagger \hat{t}'_{ij} d_j + \text{H.c.}]$, where $\langle ij \rangle$ and $\langle\langle ij \rangle\rangle$ denote the nearest-neighbor (NN) and next-nearest-neighbor (NNN) sites, respectively, $d \equiv (d_{xy}^A, d_{x^2-y^2}^A, d_{xy}^B, d_{x^2-y^2}^B)^T$, A and B denote the sublattice, \hat{t}_{ij} and \hat{t}'_{ij} are hopping matrices with SOC included [37]. As displayed in Fig. 4(a)-4(c), the Dirac points around Γ from the band inversion are indeed gapped by SOC, while the Wilson loop calculation confirms the trivial topology consistent with symmetry consideration. Furthermore, as indicated by IR shown in Fig. 4(a), the band structure of \mathcal{H}_1 without SOC has level crossing along Γ - M , which is contrary to the first principles calculations. All of these results suggest the topology must originate from other d orbitals.

Another band inversion occurs at M between d_{xz} , d_{yz} and d_{z^2} (Fig. 3(b) right), which is about 1 eV away from the Fermi level. The calculated IR are consistent with the Elementary Band Representations (EBR) [39–43] listed in Table II. We further construct a concrete tight-binding model \mathcal{H}_2 from *nonplanar* orbitals d_{xz} , d_{yz} and d_{z^2} to decipher whether the band inversion at M contributes nontrivial topology. $\mathcal{H}_2 = \sum_{\langle ij \rangle} [c_i^\dagger \hat{h}_{ij} c_j + \text{H.c.}] + \sum_{\langle\langle ij \rangle\rangle} [c_i^\dagger \hat{h}'_{ij} c_j + \text{H.c.}]$, where $c \equiv (d_{xz}^A, d_{yz}^A, d_{z^2}^A, d_{xz}^B, d_{yz}^B, d_{z^2}^B)^T$, and \hat{h}_{ij} and \hat{h}'_{ij} are general 6×6 matrices denoting hopping terms with SOC included, which can be simplified by symmetry considerations. The explicit forms are listed in Supplementary Materials [37]. As displayed in Fig. 4(d)-4(f), we use typical parameters by matching all of the IR along symmetry lines and symmetry points with Fig. 3(b) and recover band inversion between M_2 and M_3 . The four Dirac points along Γ - M gapped by SOC contribute a total Chern number $\mathcal{C} = 4 \times 1/2 = 2$, which is consistent with Wilson loop of the two lowest bands. Thus the band inversion at M accounts for $\mathcal{C} = 2$ in monolayer ATiX.

To fully understand the band structure and topology in Fig. 3(a), we need to include all of the five d orbitals.

	Γ	X	M
d_{xy}	$\Gamma_1^-(1) \oplus \Gamma_4^+(1)$	$X_2(2)$	$M_2(2)$
$d_{x^2-y^2}$	$\Gamma_2^-(1) \oplus \Gamma_3^+(1)$	$X_1(2)$	$M_1(2)$
d_{z^2}	$\Gamma_1^+(1) \oplus \Gamma_4^-(1)$	$X_1(2)$	$M_2(2)$
d_{xz}, d_{yz}	$\Gamma_5^+(2) \oplus \Gamma_5^-(2)$	$X_1(2) \oplus X_2(2)$	$M_3(2) \oplus M_4(2)$

TABLE II. EBR without time-reversal symmetry for space group $P4/nmm$ from Wyckoff position $2a$.

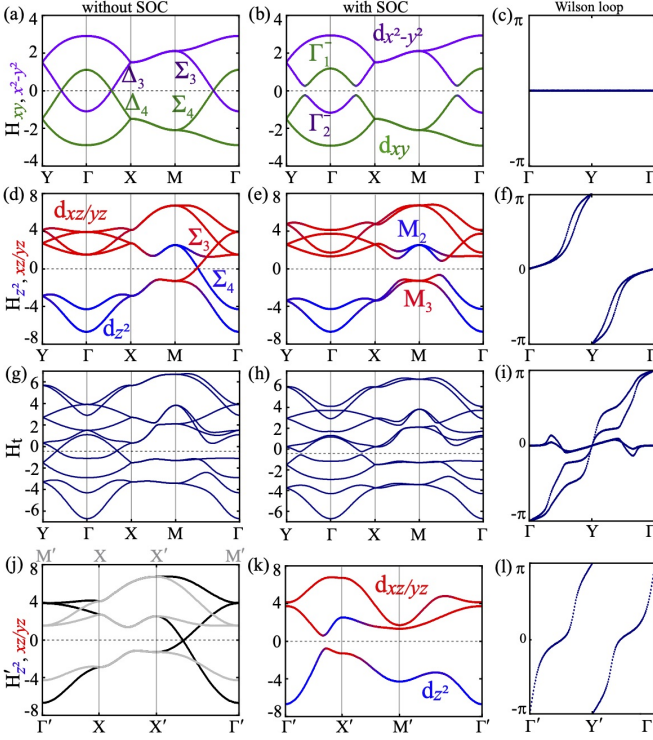


FIG. 4. The band structure and Wilson loop of the tight-binding model. (a)-(c) \mathcal{H}_1 , (d)-(f) \mathcal{H}_2 , (g)-(i) \mathcal{H} from all five d orbitals. The band structure without SOC, with SOC and Wilson loop of the lowest bands below Fermi level, respectively. The IR along symmetry lines and at symmetry points in (a) and (d) are consistent with that in Fig. 3(b). (j)-(l) The band structure of \mathcal{H}'_2 from $(d_{xz}, d_{yz}, d_{z^2})$ in the new unit cell with SOC, without SOC and Wilson loop of the lowest band, respectively.

From the above analysis, \mathcal{H}_1 from $(d_{xy}, d_{x^2-y^2})$ without SOC accounts for the trivial band crossing along Γ - X and Γ - Y , but it inevitably introduces level crossing along Γ - M . \mathcal{H}_2 from $(d_{xz}, d_{yx}, d_{z^2})$ without SOC accounts for the topological band inversion at M , but it inevitably introduces level crossing along Γ - M . As shown in Fig. 4(a) and 4(d), the IRs of the two crossed bands along Γ - M are Σ_3 and Σ_4 in \mathcal{H}_1 , which is just the opposite to that in \mathcal{H}_2 . This symmetry analysis simply indicates by including inter-orbital hopping (as \mathcal{H}_{12}) between $(d_{xy}, d_{x^2-y^2})$ and $(d_{xz}, d_{yx}, d_{z^2})$, the symmetry protected band crossing along Γ - M will be gapped even in the absence of SOC. This is clearly demonstrated in Fig. 4(g) for $\mathcal{H} = \mathcal{H}_1 + \mathcal{H}_2 + \mathcal{H}_{12}$ without SOC [37], which leaves the Dirac points along Γ - X and Γ - Y only. Then putting the SOC back, we see a full gap opening in Fig. 4(h), and the Wilson loop for the lowest four band is topological which is equal to the direct sum of Fig. 4(c) and Fig. 4(f). There is a subtlety point in Fig. 3(a) worth mentioning, that at Γ the two-fold degenerate IR $\Gamma_5^-(2)$ from d_{xz}, d_{yz} energetically lies below $\Gamma_1^+(1) \oplus \Gamma_4^-(1)$ from d_{z^2} . This will not affect the topology due to opposite an-

gular momentum from $d_{xz} \pm id_{yz}$. Now, we understand the essential physics and reproduce the main result in Fig. 3(a) and 3(b) by a five d -orbital model in Fig. 4(h). Since the topological band inversion is contributed by d_{xz}, d_{yx} , and d_{z^2} far away from Fermi level, the chiral edge states always exist irrespective of the band crossing or gap opening along Γ - X (Y). This explains the edge states in Fig. 2(h) for FM along x axis.

Finally, we provide an intuitive understanding why the band inversion from (d_{xz}, d_{yz}) and d_{z^2} at M leads to high Chern number $\mathcal{C} = 2$. For the unit cell in Fig. 1(b), the elements at Wyckoff position $2c$ introduce the difference between A and B sublattice of Ti at Wyckoff position $2a$. Since the topology is purely from the d orbitals of Ti, if we ignore the difference between A and B sublattices, we can construct a new square lattice with the unit cell containing a single Ti atom (gray dash line in Fig. 3(c)). The relation between unfolded (labelled by Γ' - X' - Y' - M') and original Brillouin zone is also displayed. Now we can rewrite \mathcal{H}_2 in the new unit cell as \mathcal{H}'_2 from nonplanar orbitals d_{xz}, d_{yz} and d_{z^2} only [37], and replot the band structure. As shown in Fig. 4(j), the band structure without SOC along Γ' - X' - X' - Γ' (black line) together with M' - X' - X' - M' (gray line) almost reproduces the band features in Fig. 4(d), i.e., the band structure of \mathcal{H}_1 is almost the folding of that of \mathcal{H}'_1 . According to band folding picture, the band inversion at M in the original Brillouin zone now is related to band inversion at X' in the unfolded Brillouin zone as shown in Fig. 4(k). There is C_{2z} rotational symmetry at X' , so the band inversion between angular momentum $\ell_z = \pm 1$ of d_{xz}, d_{yz} and $\ell_z = 0$ of d_{z^2} at X' is similar to a s - p band inversion with $\mathcal{C} = 1$. The same band inversion also happens around Y' from C_{4z} with another $\mathcal{C} = 1$. Then the total Chern number is $\mathcal{C} = 1 + 1 = 2$, which is consistent with the Wilson loop calculation in Fig. 4(l). Now both X' and Y' are folded into M without gap closing, then the total Chern number of the folded bands below Fermi level remains the same.

Generalization and discussion. The model and analysis from d orbitals above are general, and also apply to the previous reported $\mathcal{C} = 2$ QAH insulator in monolayer TiTe [23], LiFeSe [22], FeI [24] with similar d -orbital projected band structure and IR (Fig. S9 [37]), where the origin of topology from (d_{xz}, d_{yz}) and d_{z^2} at M were overlooked. The topological physics in TiTe is from d -orbitals of Ti at Wyckoff position $2a$ of space group $P4/nmm$, which is in the $e_g^{\uparrow 2} t_{2g}^{\uparrow 0}$ configuration with occupied d_{xy} and d_{z^2} for majority spin in the polarized state. While in LiFeSe [22] and FeI [24], each Fe takes the Wyckoff position $2a$ of $P4/nmm$ and is in the $e_g^{\uparrow 4} t_{2g}^{\uparrow 3} = e_g^{\uparrow 2} t_{2g}^{\uparrow 3} e_g^{\downarrow 2} t_{2g}^{\downarrow 0}$ configuration. The e_g - t_{2g} kinetic exchange leads to ultra-stable FM, and the system is in a spin polarized state with occupied d_{xy} and d_{z^2} for minority spin. The similar polarized $e_g^2 t_{2g}^0$ configuration with C_{4z} rotational symmetry in all of these materials (Ti or Fe lattices) give rise

Space group	$P4/nmm$	$P-42m$
Subgroup	$P4/n, P4_212, P-4m2, P-42_1m$	N/A

TABLE III. Two typical layer groups and their subgroups which are compatible with distorted tetrahedral crystal field and C_{4z} rotational symmetry.

to $\mathcal{C} = 2$ QAH phase with the same origin of topology.

The key ingredient for the $\mathcal{C} = 2$ phase is the polarized $e_g^2 t_{2g}^0$ configuration of d orbitals, which is generated by the distorted tetrahedral crystal field by ligands at Wyckoff position $2c$. The distortion of tetrahedron will lift the degeneracy within t_{2g} and e_g , and determine the splitting and relative energetics between planar and nonplanar orbitals (Fig. S10 [37]). As long as the crystal field splitting is small compared to the d orbital band width, the five d orbital model here always works, namely, d_{xz}, d_{yz} and d_{z^2} give rise to the topological band inversion. Here we suggest several layer groups in Table III, which are compatible with such a crystal field and have square lattice structure with C_{4z} symmetry. For example, the most simple structures are $P-4m2$ and $P-42m$ shown in Fig. 3(d). We propose similar electronic structure with same topological properties can be found in transition metal compounds with these space groups, when the d orbital configuration $e_g^2 t_{2g}^0$ is fulfilled. Interestingly, the octahedral crystal field could also lead to t_{2g} and e_g splitting with opposite energy sequence, the polarized $t_{2g}^3 e_g^0$ configuration of d orbitals together with C_{4z} from certain transition metal may also lead to $\mathcal{C} = 2$ QAH phase, the concrete material family is left for future study.

In summary, our work uncover $\mathcal{C} = 2$ QAH phase from $3d$ orbitals which applies to a large class of materials in the space group $P4/nmm$. We hope the theoretical work here can aid the search for new QAH insulators in transition metal compounds.

Acknowledgment. This work is supported by the National Key Research Program of China under Grant No. 2019YFA0308404, the Natural Science Foundation of China through Grant No. 12174066, Science and Technology Commission of Shanghai Municipality under Grant No. 20JC1415900, the Innovation Program for Quantum Science and Technology through Grant No. 2021ZD0302600, Shanghai Municipal Science and Technology Major Project under Grant No. 2019SHZDZX01.

* Corresponding author: wjingphys@fudan.edu.cn

- [1] M. Z. Hasan and C. L. Kane, “*Colloquium*: Topological insulators,” *Rev. Mod. Phys.* **82**, 3045–3067 (2010).
 [2] Xiao-Liang Qi and Shou-Cheng Zhang, “Topological insulators and superconductors,” *Rev. Mod. Phys.* **83**,

1057–1110 (2011).

- [3] Yoshinori Tokura, Kenji Yasuda, and Atsushi Tsukazaki, “Magnetic topological insulators,” *Nature Rev. Phys.* **1**, 126–143 (2019).
 [4] Jing Wang and Shou-Cheng Zhang, “Topological states of condensed matter,” *Nature Mat.* **16**, 1062–1067 (2017).
 [5] Cui-Zu Chang, Chao-Xing Liu, and Allan H. MacDonald, “Colloquium: Quantum anomalous hall effect,” *arXiv: 2202.13902* (2022), 10.48550/ARXIV.2202.13902.
 [6] B. Andrei Bernevig, Claudia Felser, and Haim Beidenkopf, “Progress and prospects in magnetic topological materials,” *Nature* **603**, 41–51 (2022).
 [7] D. J. Thouless, M. Kohmoto, M. P. Nightingale, and M. den Nijs, “Quantized hall conductance in a two-dimensional periodic potential,” *Phys. Rev. Lett.* **49**, 405–408 (1982).
 [8] F. D. M. Haldane, “Model for a quantum hall effect without landau levels: Condensed-matter realization of the “parity anomaly”,” *Phys. Rev. Lett.* **61**, 2015–2018 (1988).
 [9] Cui-Zu Chang, Jinsong Zhang, Xiao Feng, Jie Shen, Zuocheng Zhang, Minghua Guo, Kang Li, Yunbo Ou, Pang Wei, Li-Li Wang, Zhong-Qing Ji, Yang Feng, Shuaihua Ji, Xi Chen, Jinfeng Jia, Xi Dai, Zhong Fang, Shou-Cheng Zhang, Ke He, Yayu Wang, Li Lu, Xu-Cun Ma, and Qi-Kun Xue, “Experimental Observation of the Quantum Anomalous Hall Effect in a Magnetic Topological Insulator,” *Science* **340**, 167–170 (2013).
 [10] Cui-Zu Chang, Weiwei Zhao, Duk Y. Kim, Haijun Zhang, Badih A. Assaf, Don Heiman, Shou-Cheng Zhang, Chaoxing Liu, Moses H. W. Chan, and Jagadeesh S. Moodera, “High-precision realization of robust quantum anomalous hall state in a hard ferromagnetic topological insulator,” *Nature Mater.* **14**, 473 (2015).
 [11] M. Mogi, R. Yoshimi, A. Tsukazaki, K. Yasuda, Y. Kozuka, K. S. Takahashi, M. Kawasaki, and Y. Tokura, “Magnetic modulation doping in topological insulators toward higher-temperature quantum anomalous hall effect,” *Appl. Phys. Lett.* **107**, 182401 (2015).
 [12] A. J. Bestwick, E. J. Fox, Xufeng Kou, Lei Pan, Kang L. Wang, and D. Goldhaber-Gordon, “Precise quantization of the anomalous hall effect near zero magnetic field,” *Phys. Rev. Lett.* **114**, 187201 (2015).
 [13] R. Watanabe, R. Yoshimi, M. Kawamura, M. Mogi, A. Tsukazaki, X. Z. Yu, K. Nakajima, K. S. Takahashi, M. Kawasaki, and Y. Tokura, “Quantum anomalous hall effect driven by magnetic proximity coupling in all-telluride based heterostructure,” *Appl. Phys. Lett.* **115**, 102403 (2019).
 [14] Yujun Deng, Yijun Yu, Meng Zhu Shi, Zhongxun Guo, Zihan Xu, Jing Wang, Xian Hui Chen, and Yuanbo Zhang, “Quantum anomalous hall effect in intrinsic magnetic topological insulator mnbi₂te₄,” *Science* **367**, 895–900 (2020).
 [15] M. Serlin, C. L. Tschirhart, H. Polshyn, Y. Zhang, J. Zhu, K. Watanabe, T. Taniguchi, L. Balents, and A. F. Young, “Intrinsic quantized anomalous hall effect in a moiré heterostructure,” *Science* **367**, 900–903 (2020).
 [16] Tingxin Li, Shengwei Jiang, Bowen Shen, Yang Zhang, Lizhong Li, Zui Tao, Trithep Devakul, Kenji Watanabe, Takashi Taniguchi, Liang Fu, Jie Shan, and Kin Fai Mak, “Quantum anomalous hall effect from intertwined moiré bands,” *Nature* **600**, 641–646 (2021).

- [17] Xiao-Liang Qi, Taylor L. Hughes, and Shou-Cheng Zhang, “Chiral topological superconductor from the quantum hall state,” *Phys. Rev. B* **82**, 184516 (2010).
- [18] Jing Wang, Quan Zhou, Biao Lian, and Shou-Cheng Zhang, “Chiral topological superconductor and half-integer conductance plateau from quantum anomalous hall plateau transition,” *Phys. Rev. B* **92**, 064520 (2015).
- [19] Biao Lian, Xiao-Qi Sun, Abolhassan Vaezi, Xiao-Liang Qi, and Shou-Cheng Zhang, “Topological quantum computation based on chiral majorana fermions,” *Proc. Natl. Acad. Sci. USA* **115**, 10938–10942 (2018).
- [20] Jing-Yang You, Zhen Zhang, Bo Gu, and Gang Su, “Two-dimensional room-temperature ferromagnetic semiconductors with quantum anomalous hall effect,” *Phys. Rev. Applied* **12**, 024063 (2019).
- [21] Jiaxiang Sun, Xin Zhong, Wenwen Cui, Jingming Shi, Jian Hao, Meiling Xu, and Yinwei Li, “The intrinsic magnetism, quantum anomalous hall effect and curie temperature in 2d transition metal trihalides,” *Phys. Chem. Chem. Phys.* **22**, 2429–2436 (2020).
- [22] Yang Li, Jiaheng Li, Yang Li, Meng Ye, Fawei Zheng, Zetao Zhang, Jingheng Fu, Wenhui Duan, and Yong Xu, “High-temperature quantum anomalous hall insulators in lithium-decorated iron-based superconductor materials,” *Phys. Rev. Lett.* **125**, 086401 (2020).
- [23] X. Xuan, Z. Zhang, C. Chen, and W. Guo, “Robust quantum anomalous hall states in monolayer and few-layer tite,” *Nano Lett.* **22**, 5379–5384 (2022).
- [24] Qilong Sun, Yandong Ma, and Nicholas Kioussis, “Two-dimensional dirac spin-gapless semiconductors with tunable perpendicular magnetic anisotropy and a robust quantum anomalous hall effect,” *Mater. Horiz.* **7**, 2071–2077 (2020).
- [25] Zeyu Li, Yulei Han, and Zhenhua Qiao, “Chern number tunable quantum anomalous hall effect in monolayer transitional metal oxides via manipulating magnetization orientation,” *Phys. Rev. Lett.* **129**, 036801 (2022).
- [26] Chao-Xing Liu, Xiao-Liang Qi, Xi Dai, Zhong Fang, and Shou-Cheng Zhang, “Quantum anomalous hall effect in $\text{Hg}_{1-y}\text{Mn}_y\text{Te}$ quantum wells,” *Phys. Rev. Lett.* **101**, 146802 (2008).
- [27] Rui Yu, Wei Zhang, Hai-Jun Zhang, Shou-Cheng Zhang, Xi Dai, and Zhong Fang, “Quantized Anomalous Hall Effect in Magnetic Topological Insulators,” *Science* **329**, 61–64 (2010).
- [28] Jing Wang, Biao Lian, and Shou-Cheng Zhang, “Quantum anomalous hall effect in magnetic topological insulators,” *Phys. Scr.* **T164**, 014003 (2015).
- [29] Dongqin Zhang, Minji Shi, Tongshuai Zhu, Dingyu Xing, Haijun Zhang, and Jing Wang, “Topological axion states in the magnetic insulator mnbi_2te_4 with the quantized magnetoelectric effect,” *Phys. Rev. Lett.* **122**, 206401 (2019).
- [30] Jiaheng Li, Yang Li, Shiqiao Du, Zun Wang, Bing-Lin Gu, Shou-Cheng Zhang, Ke He, Wenhui Duan, and Yong Xu, “Intrinsic magnetic topological insulators in van der waals layered mnbi_2te_4 -family materials,” *Sci. Adv.* **5**, eaaw5685 (2019).
- [31] M. M. Otrokov, I. P. Rusinov, M. Blanco-Rey, M. Hoffmann, A. Yu. Vyazovskaya, S. V. Eremeev, A. Ernst, P. M. Echenique, A. Arnau, and E. V. Chulkov, “Unique thickness-dependent properties of the van der waals interlayer antiferromagnet mnbi_2te_4 films,” *Phys. Rev. Lett.* **122**, 107202 (2019).
- [32] Yi Xue Chong, Xiaolong Liu, Rahul Sharma, Andrey Kostin, Genda Gu, K. Fujita, J. C. Séamus Davis, and Peter O. Sprau, “Severe dirac mass gap suppression in sb_2te_3 -based quantum anomalous hall materials,” *Nano Lett.* **20**, 8001–8007 (2020).
- [33] M. Garnica, M. M. Otrokov, P. Casado Aguilar, I. I. Klimovskikh, D. Estyunin, Z. S. Aliev, I. R. Amiraslanov, N. A. Abdullayev, V. N. Zverev, M. B. Babanly, N. T. Mamedov, A. M. Shikin, A. Arnau, A. L. Vázquez de Parga, E. V. Chulkov, and R. Miranda, “Native point defects and their implications for the dirac point gap at $\text{mnbi}_2\text{te}_4(0001)$,” *npj Quantum Mater.* **7**, 7 (2022).
- [34] M I Aroyo, J M Perezmato, C Capillas, E Kroumova, Svetoslav Ivantchev, G Madariaga, A Kirov, and Hans Wondratschek, “Bilbao crystallographic server: I. databases and crystallographic computing programs,” *Z. Krist.* **221**, 15–27 (2006).
- [35] Asen Kirov, Cesar Capillas, J Perez-Mato, and Hans Wondratschek, “Bilbao crystallographic server. ii. representations of crystallographic point groups and space groups,” *Acta Cryst.* **62**, 115–28 (2006).
- [36] J. Perez-Mato, D Orobengoa, Emre Tasci, Gemma De la Flor Martin, and A Kirov, “Crystallography online: Bilbao crystallographic server,” *Bulg. Chem. Commun.* **43**, 183–197 (2011).
- [37] See Supplemental Material for methods and technical details.
- [38] Daniel I. Khomskii, *Transition Metal Compounds* (Cambridge University Press, 2004).
- [39] Jorrit Kruthoff, Jan de Boer, Jasper van Wezel, Charles L. Kane, and Robert-Jan Slager, “Topological classification of crystalline insulators through band structure combinatorics,” *Phys. Rev. X* **7**, 041069 (2017).
- [40] Barry Bradlyn, L Elcoro, Jennifer Cano, MG Vergniory, Zhijun Wang, C Felser, MI Aroyo, and B Andrei Bernevig, “Topological quantum chemistry,” *Nature* **547**, 298 (2017).
- [41] M. G. Vergniory, L. Elcoro, Zhijun Wang, Jennifer Cano, C. Felser, M. I. Aroyo, B. Andrei Bernevig, and Barry Bradlyn, “Graph theory data for topological quantum chemistry,” *Phys. Rev. E* **96**, 023310 (2017).
- [42] L. Elcoro, Barry Bradlyn, Z. Wang, M. G. Vergniory, Jennifer Cano, C. Felser, B. Bernevig, D. Orobengoa, G. D. L. Flor, and M. Aroyo, “Double crystallographic groups and their representations on the bilbao crystallographic server,” *J. Appl. Crystallogr* **50**, 1457 (2017).
- [43] Adrien Bouhon, Gunnar F. Lange, and Robert-Jan Slager, “Topological correspondence between magnetic space group representations and subdimensions,” *Phys. Rev. B* **103**, 245127 (2021).